# Progress in simulating turbulent electron thermal transport in NSTX



2013 Nucl. Fusion 53 093022

(http://iopscience.iop.org/0029-5515/53/9/093022)

IOP Publishing and International Atomic Energy Agency — Nuclear Fusion

Nucl. Fusion **53** (2013) 093022 (13pp) doi:10.1088/0029-5515/53/9/093022

# Progress in simulating turbulent electron thermal transport in NSTX

**W. Guttenfelder[1], J.L. Peterson[2], J. Candy[3], S.M. Kaye[1], Y. Ren[1], R.E. Bell[1], G.W. Hammett[1], B.P. LeBlanc[1], D.R. Mikkelsen[1], W.M. Nevins[2] and H. Yuh[4]**

[1] Princeton Plasma Physics Laboratory, Princeton, NJ 08543, USA
[2] Lawrence Livermore National Laboratory, Livermore, CA 94551, USA
[3] General Atomics, San Diego, CA 92186, USA
[4] Nova Photonics Inc., Princeton, NJ 08540, USA

E-mail: wgutten@pppl.gov

Received 2 January 2013, accepted for publication 26 July 2013
Published 21 August 2013
Online at stacks.iop.org/NF/53/093022

**Abstract**

Nonlinear simulations based on multiple NSTX discharge scenarios have progressed to help differentiate unique instability mechanisms and to validate with experimental turbulence and transport data. First nonlinear gyrokinetic simulations of microtearing turbulence in a high-beta NSTX H-mode discharge predict experimental levels of electron thermal transport that are dominated by magnetic flutter and increase with collisionality, roughly consistent with energy confinement times in dimensionless collisionality scaling experiments. Electron temperature gradient (ETG) simulations predict significant electron thermal transport in some low- and high-beta discharges when ion scales are suppressed by $E \times B$ shear. Although the predicted transport in H-modes is insensitive to variation in collisionality (inconsistent with confinement scaling), it is sensitive to variations in other parameters, particularly density gradient stabilization. In reversed shear L-mode discharges that exhibit electron internal transport barriers, ETG transport has also been shown to be suppressed nonlinearly by strong negative magnetic shear, $s \ll 0$. In many high-beta plasmas, instabilities which exhibit a stiff beta dependence characteristic of kinetic ballooning modes (KBMs) are sometimes found in the core region. However, they do not have a distinct finite beta threshold, instead transitioning gradually to a trapped electron mode (TEM) as beta is reduced to zero. Nonlinear simulations of this 'hybrid' TEM/KBM predict significant transport in all channels, with substantial contributions from compressional magnetic perturbations. As multiple instabilities are often unstable simultaneously in the same plasma discharge, even on the same flux surface, unique parametric dependencies are discussed which may be useful for distinguishing the different mechanisms experimentally.

(Some figures may appear in colour only in the online journal)

## 1. Introduction

Developing a predictive transport capability for spherical tokamaks (STs) is an important goal for the design of future low aspect ratio fusion devices, such as an ST-based fusion nuclear science facility (FNSF) [1], component test facility (CTF) [2] or pilot plant [3]. While ion thermal transport is often neoclassical in NSTX [4–6] and MAST [7, 8] H-modes, electron thermal transport is always anomalous and can influence and limit the overall global energy confinement scaling [4–8]. To understand the cause of core anomalous electron thermal transport due to microinstabilities driven by thermal plasma gradients (we do not address here the H-mode pedestal, or transport due to energetic particle instabilities such as global or compressional Alfvén eigenmodes (GAEs/CAEs) [9–11]), nonlinear simulations are required to validate with experimental transport and turbulence measurements, and to help distinguish unique instability mechanisms, both of which can be used to improve predictive modelling capabilities.

One of the complications of developing an integrated understanding of transport in STs is the broad range of parameter space and therefore wide range of instabilities that are possible. For example, ST plasmas can span a significant range of beta, collisionality, toroidal flow/flow shear and flux surface shaping. As a result many drift wave instabilities can be predicted, which include ion temperature gradient (ITG) [12], trapped electron mode (TEM) [13], electron temperature gradient (ETG) [14], microtearing (MT) mode [15] and even kinetic ballooning modes (KBMs) [16] (the kinetic analogue to the ideal, infinite-$n$ magnetohydrodynamic (MHD) ballooning mode [17]). While the ITG, TEM and ETG instabilities exist in the purely electrostatic limit ($\beta = 0$), the MT and KBM are electromagnetic and are expected to occur at higher beta.

In particular, the MT instability has been predicted to occur in a number of high-beta ST discharges, in both NSTX [18–22] and MAST [23–25]. Perhaps somewhat unexpected is that MT has also been predicted to be unstable in the core of conventional tokamaks that operate at lower beta relative to STs. Although often co-existing with, or subdominant to ITG or TEM, such cases have now been predicted for ASDEX Upgrade [26–28], DIII-D [29] and JET [30]. MT is also predicted to occur in improved confinement regimes of reversed field pinches (RFPs) [31, 32], as well as in the pedestal region of MAST [33, 34], NSTX [35], JET [36] and even for model ITER profiles [37]. The prevalence of MT instability in such a variety of toroidal confinement devices highlights the need for nonlinear simulations to determine the nonlinearly saturated transport amplitude and fluctuation characteristics for comparison with experiments. As will be shown below, the high-beta conditions in STs provide a unique testbed to isolate the MT mode to study its influence on transport and turbulence.

Nonlinear simulations are challenging in STs as it is unknown *a priori* what instability mechanisms are theoretically most important. To capture the correct qualitative physics it is crucial to account for many effects simultaneously, including: realistic equilibrium at low aspect ratio and high-beta, fully electromagnetic perturbations (shear and compressional), collisions, multiple kinetic species, and toroidal flow and flow shear. In addition, care must be taken when selecting numerical grid resolutions to ensure that the relevant physical mechanisms can be appropriately represented (e.g. [38]). Although often numerically challenging and expensive, these investigations advance theoretical understanding of turbulent transport phenomenon, particularly at finite beta, which will improve confidence in predictions for ITER plasmas (e.g. [39]).

Here we present recent progress in simulating microturbulence based on experimental NSTX discharges, with a focus predominantly on the observed anomalous electron thermal transport. We first address linear stability results and then focus on nonlinear simulations for MT, ETG and KBM turbulence. We have employed the Eulerian delta-$f$ gyrokinetic code GYRO [40–43] as it is capable of including the physical effects listed above, all of which are expected to be important in the core confining region of NSTX plasmas. While the ultimate goal is to pursue quantitative validation of the gyrokinetic predictions with measured transport and turbulence, it is very expensive computationally to demonstrate quantitative convergence for all simulations, in particular for the high-beta MT and KBM turbulence. In these cases it is still possible to obtain qualitatively meaningful results that provide much insight, which can be used to understand the nature of high-beta core transport in STs.

## 2. Linear stability

Local, linear gyrokinetic simulations have been run for many NSTX discharges using experimentally constrained MHD equilibria and local plasma parameters. We highlight the results from a few cases to illustrate generally what drift wave instabilities are predicted to be unstable in the core confinement region. Data is used from NBI heated H-mode plasmas with varying plasma current $I_p$ (0.7–1.1 MA), toroidal field $B_T$ (0.35–0.55 T), density ($n_e = (1\text{–}6) \times 10^{19}\,\text{m}^{-3}$) and heating power ($P_{NBI} = 2\text{–}4$ MW) and are associated with the following experiments: dimensionless collisionality ($\nu_*$) scans that used boronization and helium glow discharge cleaning for wall conditioning (shot numbers 120967–121014) [4, 5]; a scan in which progressively larger amounts of lithium was deposited to the lower divertor region between shots, at constant $I_p$ and $B_T$ (129016–129041) [44–47]; a set of shots that varied $I_p$ and $B_T$ for similar amount of between-shot lithium conditioning (138550–138564) [6, 48, 49], and a separate $\nu_*$ scan (141031, 141040) [50] at lower density than the discharges of [4, 5]. For comparison, an L-mode discharge is also included (141716) [51].

To illustrate the linear stability results we use regime diagrams to relate the dominant predicted instability mechanism with relevant local parameters (figure 1) which are defined as follows [40]: local electron beta $\beta_e = 8\pi n_e T_e / B_{T0}^2$ where $B_{T0} =$ is the vacuum toroidal field at the magnetic axis; electron–ion collision frequency $\nu^{e/i} = Z_{\text{eff}} \cdot \nu_{ei}$, where $\nu_{ei} = 4\pi n_e e^4 \log \Lambda/(2T_e)^{3/2} m_e^{1/2}$; normalized electron temperature gradient, e.g. $a/L_{T_e} = -a/T_e \cdot dT_e/dr$, where $r$ is a flux surface label equal to the mid-plane minor radius for up–down symmetric surfaces (see [43] for the exact definition); MHD alpha parameter $\alpha_{\text{MHD,unit}} = -q^2 R_0 \cdot 8\pi/B_{\text{unit}}^2 \cdot dp/dr$, using the normalizing magnetic field $B_{\text{unit}} = B_T \cdot \rho/r \cdot d\rho/dr$, where $\rho = (\Psi_t/\pi B_T)^{1/2}$, $\Psi_t$ is the toroidal flux (typically $B_{\text{unit}}/B_T \sim 2$ in these cases); $E \times B$ shearing rate $\gamma_E = -r/q \cdot d\omega_0/dr$, where $\omega_0 = -d\Phi_0/d\psi$ is the toroidal rotation frequency, $\Phi_0$ is the equilibrium electric field potential and $\psi$ is the poloidal flux. Typical values of minor radius are $a \approx 0.62$ m, and the local ($r/a = 0.6\text{–}0.7$) flux surface elongation ($\kappa$) and triangularities ($\delta$) ranged between $\kappa = 1.5\text{–}2.2$ and $\delta = 0.1\text{–}0.24$. The linear simulations use the GYRO initial value solver with numerical grids that have been shown in the past to provide good quantitative accuracy for microinstabilities that arise in NSTX ($n_\lambda = 12$ pitch angles, $n_E = 8$ energies, $n_\theta = 14$ parallel orbit mesh points $\times$ 2 signs of parallel velocity, and $n_r = 16\text{–}32$ radial grid points). In particular, the relatively large number of radial grid points is required to resolve the narrow parallel current layer that is fundamental to the MT instability [28, 52–55].

We emphasize that the plots in figure 1 are used to illustrate a correlation of where in experimental parameter space particular linear instabilities are predicted to occur. They do not represent formal stability boundaries that would require varying one parameter at a time while keeping all other parameters fixed. Furthermore, we use parameters between $r/a = 0.6\text{–}0.7$ as there tends to be a reasonable correlation between the local electron thermal diffusivities in this region and the overall energy confinement times [6, 45].

Linear analysis of NSTX high-beta discharges show that MT modes at ion gyroradius scale lengths ($k_\theta \rho_s < 1$) are often unstable and are driven by the electron temperature gradient at sufficiently large electron beta, which for these H-mode locations can be characterized by $\beta_e > 4\%$ (figure 1($a$)). (See [22, 55] for example linear spectra and mode structures.)

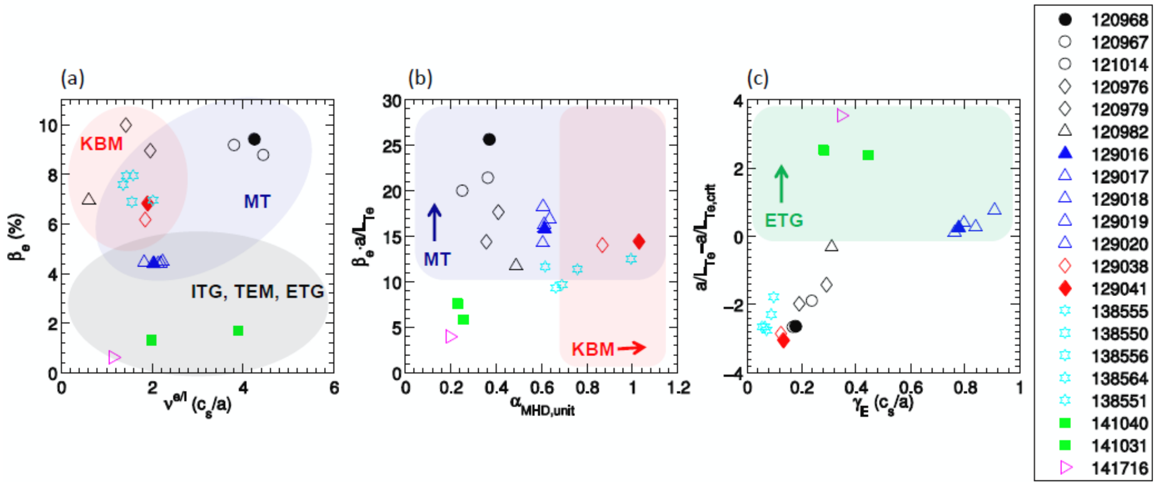


**Figure 1.** Local parameters ($r/a = 0.6$–$0.7$) for various NSTX H-mode discharges including (*a*) $\beta_e$ versus $\nu^{e/i}$, (*b*) $\beta_e \cdot a/L_{T_e}$ versus $\alpha_{MHD}$ and (*c*) $a/L_{T_e} - a/L_{T_{e,crit,ETG}}$ versus $\gamma_E \cdot a/c_s$ (see text for definitions). Shaded regions indicate where in parameter space particular microinstabilities are predicted to occur based on linear gyrokinetic simulations.

MT also tends to be stronger at higher electron–ion collision frequency when found in the core, although there are additional dependences with safety factor ($q$), magnetic shear ($s$) and density gradient [22]. For the lower density (and overall lower beta) H-mode discharges (141031,40) as well as the L-mode discharge, MT modes are stable, and instead traditional electrostatic ITG and TEM instabilities are predicted (see [50, 51] for example linear spectra).

For some of the high-beta discharges a KBM instability is also predicted (which will be discussed further in section 5), but generally only for relatively smaller electron collision frequencies. While KBM is hypothesized to be a possible mechanism for constraining the maximum H-mode pedestal pressure gradient (e.g. [56, 57]), the locations investigated here are in the core confining region, not in the sharp gradient region of the pedestal, suggesting that KBM turbulence could be an additional mechanism controlling core confinement in NSTX at lower collisionality. A transition in dominant regimes from MT to KBM would presumably influence the overall energy confinement scaling and its dependence on collisionality [6]. Understanding this dependence is of high priority for NSTX Upgrade [58, 59], and being able to predict it would be useful for the design of future ST devices.

While it is of interest to understand experimentally when different instabilities are predicted to occur in experimental $\beta_e$–$\nu_e$ space as shown in figure 1(*a*), the linear instabilities are driven by gradients in the density and temperature and often exhibit thresholds in these parameters. For example, MT has been shown to have thresholds in both $\beta_e$ and $a/L_{T_e}$ [22, 25] and slab theory suggests that a useful identifying parameter is given by the product $\beta_e \cdot a/L_{T_e}$ [53]. For these NSTX H-mode examples a rough criteria for instability appears to be $\beta_e \cdot a/L_{T_e} > 10\%$ (figure 1(*b*)). For KBM, theory predicts that $\alpha_{MHD}$ is a useful threshold parameter as it is driven by the total pressure gradient [16, 17, 56, 57]. For the NSTX H-modes KBM is often predicted to occur when $\alpha_{MHD}$ approaches unity (for the definition above). Although $\beta_e$ for 120968 ($r/a = 0.6$) is larger than that for 129041 ($r/a = 0.7$) (figure 1(*a*), filled circle and diamond, respectively), KBM dominates in the latter case because $\alpha_{MHD}$ is $\sim 3\times$ larger (figure 1(*b*)). This increased value of $\alpha_{MHD}$ is largely a consequence of the increased local density gradients in the lithiated discharges [44] which contribute substantially to the total pressure gradient. The slightly larger value of $q$ at $r/a = 0.7$ (120941) compared to $r/a = 0.6$ (120968) also increases $\alpha_{MHD}$. Obviously the exact MT and KBM thresholds will depend on other parameters such as magnetic shear and collisionality, which will vary for each discharge.

In addition to the ion scale drift waves (ITG, TEM, KBM, MT), the ETG instability at electron gyroradius scale lengths ($k_\theta \rho_s \gg 1$, $k_\theta \rho_e \leqslant 1$) is sometimes predicted. For high aspect ratio ($\varepsilon = r/R \ll 1$), low-beta equilibria the ETG stability threshold is well characterized by $(R/L_{T_e})_{crit,ETG} = \max\{(1 + Z_{eff}T_e/T_i) \times (1.3 + 1.9s/q) \times (1 - 1.5\varepsilon), 0.8R/L_n\}$ [60]. While not strictly valid for low aspect ratio and high beta, this expression has previously been demonstrated through linear gyrokinetic simulations to provide a reasonable approximation even for NSTX cases [61, 62]. As expected, the occurrence of the ETG instability is strongly correlated with the cases when the local electron temperature gradient surpasses the analytic ETG threshold (figure 1(*c*)). It is also correlated with the local normalized $E \times B$ shearing rate becoming relatively large ($\gamma_E \cdot \alpha/c_s > 0.2$) compared to the typical ion scale linear growth rates ($\gamma_{lin,ion} \sim 0.1$–$0.3c_s/a$), consistent with the expectation that strong $E \times B$ shear ($\gamma_E > \gamma_{lin}$) should suppress ion scale turbulence [63, 64].

It is important to note that the above discussion provides one relatively simple perspective on how to interpret the calculated linear stability trends in NSTX H-modes. Exact quantitative thresholds have not been calculated for each type of instability. As indicated in figure 1, when particular instabilities are found to dominate is generally correlated with the respective gradient parameters becoming sufficiently large, e.g., $\beta_e \cdot a/L_{T_e}$ for MT, $\alpha_{MHD}$ for KBM, and $a/L_{T_e}$ for ETG, but each threshold depends on other local quantities such as $q$, $s$ and $a/L_n$. Many of these dependences have been reported elsewhere. Furthermore, as we will see below, it is rare for only one type of instability to be unstable in a given

NSTX discharge, or even at one location. To investigate the resulting nonlinear turbulence from each of these mechanisms, the remainder of the paper will focus mostly on the discharges indicated by solid symbols in figure 1.

## 3. Microtearing turbulence

First nonlinear gyrokinetic simulations of MT turbulence have recently been reported for both NSTX [55, 65] and for ASDEX Upgrade parameters [28, 66]. The NSTX simulations have been based on one of the high-$\beta$, high-$\nu$ discharges in figure 1(*a*) (120968, $r/a = 0.6$). This particular case provides a somewhat idealized condition that MT is the only unstable mode and offers the possibility to isolate its effects experimentally. As will be shown later, this is not always the case as other ion scale instabilities can often be present simultaneously, further complicating the interpretation.

We summarize here some of the key features of the nonlinear MT simulations [55, 65] that used kinetic deuterium and electron species, $\varphi$ and $A_\parallel$ perturbations, but did not include flow or flow shear. The simulations predict significant electron thermal transport, $\chi_{\mathrm{e,sim}} \approx 1.2\ \rho_s c_s^2/a = 6\,\mathrm{m^2\,s^{-1}}$ comparable to experiment $\chi_{\mathrm{e,exp}} = 5$–$8\,\mathrm{m^2\,s^{-1}}$, with a well-defined spectral peak around $k_\theta\rho_s \approx 0.25$ (or toroidal mode number $n \approx 12$, $k_\theta = nq/r$). A unique feature of these simulations compared to traditional ITG or TEM turbulence is that nearly all of the electron thermal transport (∼98%) comes from magnetic flutter ($Q_{\mathrm{e,em}} \sim v_{\parallel,\mathrm{e}} \cdot \delta B_r/B_0$) due to the strong magnetic fluctuations with $\delta B_r/B_0 \approx 0.08\%$ rms. A test-particle stochastic transport model [67], based on a Rechester–Rosenbluth magnetic diffusivity [68] calculated using the saturated magnetic perturbations directly from the simulations, is able to reproduce the order-of-magnitude transport. Consistent with the interpretation of stochastic transport, there is negligible particle, ion thermal or momentum transport as ions are much heavier than electrons ($v_{\parallel,\mathrm{i}} \ll v_{\parallel,\mathrm{e}}$). The magnetic fluctuations are strongly localized to the outboard side and calculations using a synthetic diagnostic approach predict measurable phase shifts from a polarimetry diagnostic [69, 70] to be installed on NSTX Upgrade [58, 59]. The density perturbations exhibit narrow radial corrugations (also distinct from ITG, TEM), which is directly coupled to the rational surface separation ($\Delta r_{\mathrm{rat}} = 1/nq' = 1/k_\theta \cdot s$) of the dominant toroidal modes in the nonlinear spectra.

Another interesting feature of the nonlinear simulations is that the predicted transport increases with collisionality (figure 2, dots) with a scaling ($\chi_{\mathrm{e,sim}} \sim \nu_{\mathrm{e}}^{1.1}$) [55] that is roughly consistent with global energy confinement scaling in NSTX [4–6], $\Omega_{\mathrm{i}}\tau_E \sim \nu_*^{-(0.8-0.95)}$. Although overly simplistic, the correlation between predicted local transport and global energy confinement provides an indication that MT modes could play a role in determining confinement scaling in high-beta NSTX plasmas. Furthermore, it was shown in [6] that for the $\nu_*$ scans the local experimental electron thermal diffusivities in this same spatial region is strongly correlated with the global confinement scaling, very similar to the trend in figure 2.

One of the caveats of these simulations [55] is that including the experimental value of $E \times B$ shear in the simulations ($\gamma_{E,\mathrm{exp}} \approx 0.17 c_s/a$, comparable to the maximum linear growth rate) reduces the predicted transport significantly.

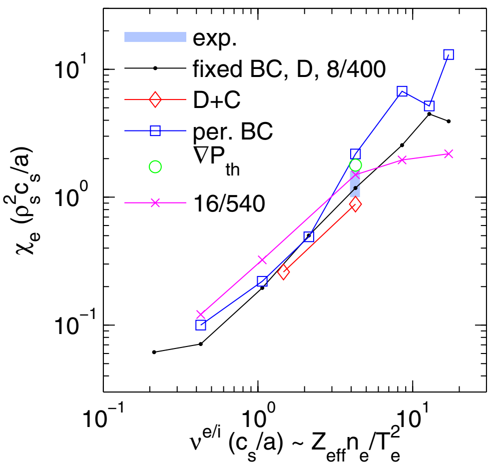


**Figure 2.** MT transport versus normalized electron–ion collision rate for different numerical and physical assumptions: (black dots) base case with deuterium only, using fixed BCs; (red diamonds) deuterium and carbon; (blue squares) periodic BCs; (green circle) thermal pressure gradient in the local equilibrium representation; (magenta crosses) higher spatial grid resolution. The blue shaded region indicates the experimental range of $\chi_{\mathrm{e}}$ and $\nu^{\mathrm{e/i}}$.

It is quite possible that the simulations are not quantitatively converged, which would influence the magnitude of transport. As discussed in depth in [55], to obtain well-behaved, spectrally saturated simulations that avoid nonphysical pile-up at high-$k$ [71] it is necessary to resolve the narrow parallel current perturbations that are fundamentally responsible for the linear MT instability. For example, for a perpendicular box size of $L_x \times L_y = 80 \times 60\rho_s$ the nonlinear simulations above used $n_x = 400$ radial grid points and $n_y = 8$ complex toroidal modes ($k_\theta\rho_{s,\mathrm{max}} = 0.735$). This provides resolution ($\Delta x = 0.2\rho_s$) that is just sufficient to represent the current perturbations associated with the highest order rational surfaces in the computational domain, which are separated by $\Delta r_{\mathrm{rat}}/\rho_s = 1/(s \cdot k_\theta\rho_{s,\mathrm{max}}) = 0.8\rho_s$ (for $s = 1.7$). A limited set of higher resolution simulations ($L_x \times L_y = 80 \times 100$, $n_x/n_y = 540/16$, $\Delta x = 0.15\rho_s$) were run for the collision frequency scan in figure 2 (×'s). For the baseline parameters the transport increased ∼25%, with a similar increase predicted for smaller collisionalities. The rollover of transport at increasing $\nu^{\mathrm{e/i}}$ occurs sooner than for the lower resolution parameters, and is more consistent with the rollover in linear growth rates [22], although the trend at lower $\nu^{\mathrm{e/i}}$ is more important experimentally (figure 1(*a*)).

Running simulations at increasing resolution quickly becomes impractical due to computational expense, prohibiting the demonstration of strict quantitative convergence with spatial resolution. However, additional numerical and physical model assumptions have also been tested to determine their impact on quantitative transport using the resolution above that was shown to reproduce the MT physics. The results are also shown in figure 2 and summarized as follows. The previous simulations were run with fixed boundary conditions (BCs) with damped buffer regions of width $\Delta^{\mathrm{b}} = 8\rho_s$ and damping rate $\nu^{\mathrm{b}} = 1\quad c_s/a$ [40] to more conveniently include $E \times B$ shearing effects. The $\nu_{\mathrm{ei}}$ scan (without $E \times B$ shear) was repeated using periodic BCs (figure 2, squares), with transport that follows the same scaling but at values 2–3× larger

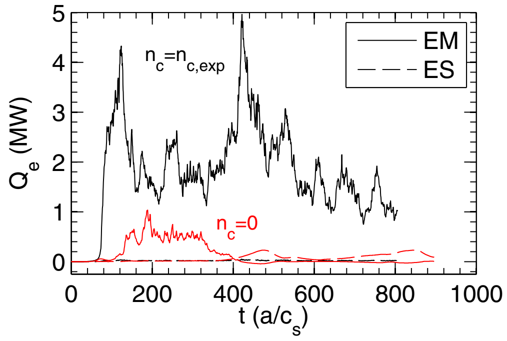


**Figure 3.** MT transport contributions from $\varphi$ (ES) and $A_{||}$ (EM) for varying carbon concentration.

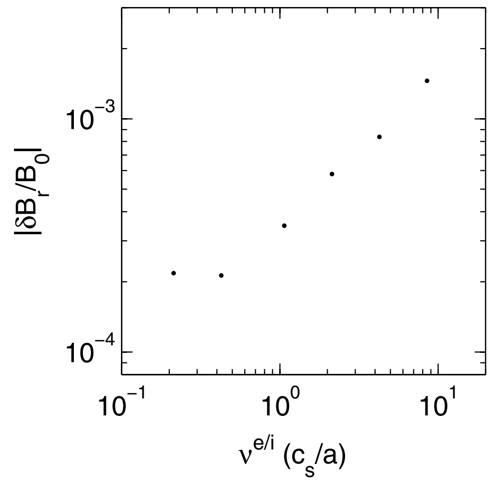


**Figure 4.** Saturated magnetic fluctuation rms amplitude $\delta B_r/B_0$ versus electron–ion collision frequency, corresponding to the black dots in figure 2.

than that with fixed boundaries. We note that both fixed and periodic BC scans exhibit strongly bursting behaviour at the highest collisionalities, likely due to the modest grid sizes. This large increase in transport with change in BC suggests that larger box sizes (specifically $L_x$) should be used, which could improve the discrepancy when including $E \times B$ shear. However, as will be discussed in section 6, nonlocal effects (due to profile variations) are likely to be important already for the $L_x = 80\rho_s$ box width.

Linear studies for this set of parameters find that MT growth rates are larger when a second (carbon) impurity species is included (due to shielding of potential perturbations from the near-adiabatic ion response [22]). Consistent with linear analysis, nonlinear simulations including a carbon ion species show transport is reduced (figure 3) as carbon concentration is reduced ($n_c \rightarrow 0$, $Z_{\rm eff} = 2.9 \rightarrow 1.0$), with the early-time averaged transport scaling similarly with collisionality (figure 2, diamonds). Later in time for the $n_c = 0$, $Z_{\rm eff} = 1$ case the turbulence appears to transition from MT with $A_{||}$ peaking at $k_\theta\rho_s \sim 0.3$, to instead a dominant electrostatic mode with $\varphi$ peaking at the lowest finite $k_\theta\rho_s = 0.1$. At these late times the ion thermal, particle and momentum fluxes are also increased due to potential perturbations. Simulations are ongoing to verify the robustness of this transition in turbulence regime to variations in numerical resolution.

The location of the above MT simulations ($r/a = 0.6$) is near the edge of the neutral beam deposition profile as calculated by the NUBEAM module in TRANSP [72]. As a result, the fast ion pressure contributes ~70% to the total pressure gradient [22] although the fast ion density is relatively small ($n_{\rm fast}/n_{\rm e} = 3.6 \times 10^{-3}$). As has been discussed previously for STs [24, 73–75], a large equilibrium pressure gradient can actually provide a strong stabilizing influence (for otherwise constant kinetic species gradients) by reducing the region of 'bad' curvature and $\nabla B$ drifts around a flux surface that is responsible for ballooning instabilities. This effect also influences the MT instability. Linear simulations show reducing the pressure gradient used in the local expansion of the Grad–Shafranov equilibrium [43] (which originally included the fast ion contribution) to match only the thermal pressure gradient ($\nabla P_{\rm th}$) increases the width and magnitude of the growth rate spectrum [22, 30]. Consequently, the resulting nonlinear transport (figure 2, circle) is >50% larger than the base case. This variation in predicted transport can be thought of as an experimental uncertainty, as the original equilibrium reconstruction was not constrained to the total pressure gradient including the calculated fast ions.

The simulations presented above illustrate a number of numerical and physical reasons why the predicted transport may not be quantitatively accurate, as the magnitude of transport around the experimental collisionality ($\nu^{e/i} = 4.2$ $c_s/a$) varies between $\chi_{\rm e} = 0.9$–$2.2$ $\rho_s^2 c_s/a$. However, in all cases the general reduction of transport at reduced $\nu^{e/i}$ is robustly confirmed, providing confidence in the expected scaling of MT transport with collisionality.

We finish the discussion of MT turbulence by noting that, in addition to the scaling with collisionality and $E \times B$ shear rate, previously published simulations predict that MT transport is sensitive to variations in electron temperature gradient and beta, exhibiting thresholds in both parameters [55]. As mentioned above, a test-particle stochastic transport model [67] is able to reproduce the order of magnitude of MT transport when using the simulated magnetic perturbations. It was shown in complementary simulations for conventional aspect ratio [28, 66] that this model holds as long as the turbulence is sufficiently strong to achieve island overlap and global stochasticity. In particular, the mixing length estimate $\delta B/B \approx \rho_{\rm e}/L_{T_{\rm e}}$ [76–78] appears to provide a reasonable model for the saturated amplitude for temperature gradients sufficiently larger than the linear threshold. However, the mixing length model cannot capture the scaling behaviour of $\delta B/B$ with other parameters such as $\nu_{\rm e}$, which does change significantly in the nonlinear simulations (figure 4). Therefore, stochastic transport models that rely on this simplified saturation estimate (e.g. [19, 20]) are incapable of reproducing the correct scaling behaviour, illustrating the importance of pursuing the nonlinear simulations and improved saturation models [28].

## 4. ETG turbulence

While the high-beta scenario in section 3 is unstable only to MT, ETG can be important in other high-beta H-modes. Linear growth rates calculated for one of the discharges discussed in

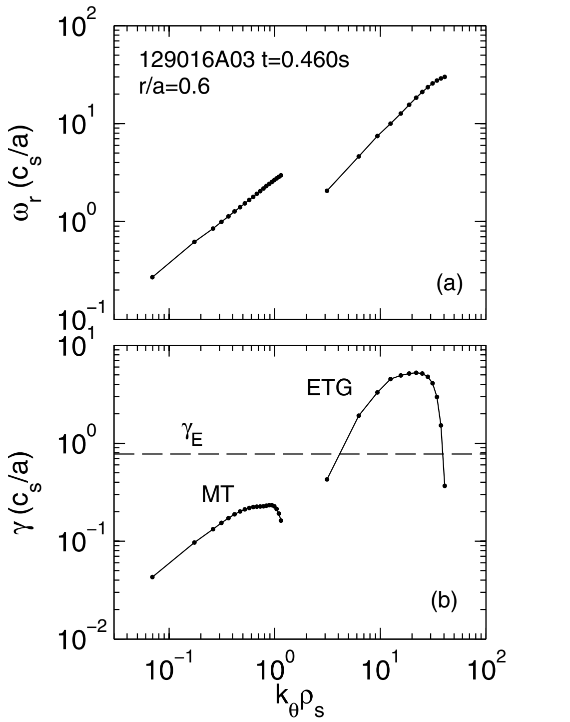


**Figure 5.** (*a*) Real frequencies and (*b*) linear growth rates for 129016 ($r/a = 0.6$). Both MT (at low $k_\theta\rho_s$) and ETG (at high $k_\theta\rho_s$) instabilities exist. The dashed line indicates the local $E \times B$ shearing rate.

section 2 (129016, $r/a = 0.6$) show that ETG is unstable at high $k_\theta\rho_s$ at the same time MT modes are unstable at low $k_\theta\rho_s$ (figure 5). However, in this case, there is very large $E \times B$ shear which is expected to suppress the low $k_\theta\rho_s$ modes ($\gamma_E \gg \gamma_{\text{lin,ion}}$) as was found for the simulations in section 3.

Nonlinear ETG simulations have been run for these parameters using numerical grids based on extensive convergence studies documented previously [50, 79] ($L_x \times L_y \approx 6 \times 4\rho_s$, $n_x = 192$, $n_y = 48$, $n_\lambda = 8$, $n_E = 8$, $n_\theta = 10 \times 2$). In particular, as opposed to the high spatial resolution requirements for the MT simulations above, it is possible to achieve quantitative convergence for the nonlinear ETG simulations, with less than ~10% variation in transport for further increase in box size or resolution. This is due to the strong low-$k_\theta$ cutoff provided by the large $E \times B$ shearing rate [79, 80]. For physical accuracy, the simulations include kinetic deuterium and carbon ions consistent with the experimental $Z_{\text{eff}} = 1.7$, collisions, $\varphi$, $A_{||}$, $B_{||}$ perturbations (although electromagnetic effects are not very important for ETG simulations [80, 81]), and $E \times B$ shear.

Figure 6 shows that the predicted nonlinear ETG heat flux for the experimental parameters ($Q_{\text{e,sim}} \sim 1.5$ MW) is a significant fraction of the experimental transport ($Q_{\text{e,exp}} \sim 2$ MW). With marginal increase in the electron temperature gradient the transport agrees with experiment within experimental uncertainties. This is a consequence of the 'stiff' behaviour of ETG transport for these parameters, where stiffness refers to a relatively large increase in predicted transport for a given change in temperature gradient [82]. The fact that the ETG transport can be so large (~MW, $\chi_e \sim 10\rho_e^2 v_{T_e}/L_{T_e}$) and stiff illustrates that it should be important in at least some locations in high-beta discharges. However, this stiffness is influenced by other parameters such as $q$ and $s$ [83], and also by density gradient which is discussed next.

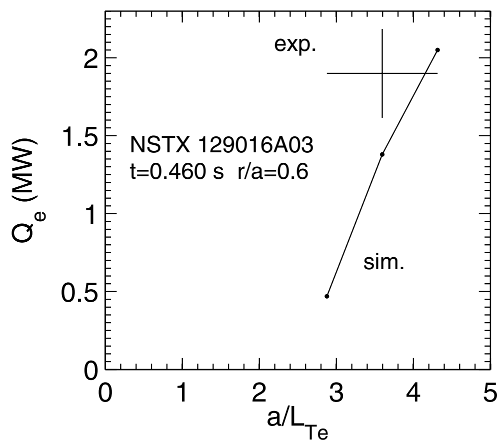


**Figure 6.** Nonlinear ETG heat flux versus temperature gradient for 129016 ($r/a = 0.6$). The experimental values with uncertainties are shown by crosshairs.

Additional experiments have been reported that attempt to validate ETG simulations with experimental transport and turbulence as measured by a 'high-$k$' coherent microwave scattering diagnostic [84]. For example, the low-beta experiments in figure 1 (141031, 141040) were carried out to vary electron collisionality ($\nu_{e*}$) by more than a factor of two with other normalized parameters kept relatively constant [50]. It was found that the measured high-$k$ spectral power (corresponding to electron scales, $k_\perp\rho_s > 3$, in the region of $r/a = 0.55$–$0.7$) appears to increase with a reduction in collisionality, even though the normalized confinement time increases as $\Omega\tau^E \sim \nu_*^{-0.8}$ (similar to high-beta $\nu_*$ scans [4, 5]). This anti-correlated dependence of the high-$k$ turbulence with confinement is counterintuitive to expectations. As discussed in section 2, MT modes are predicted to be stable in these plasmas due to the lower values of beta, and local $E \times B$ shearing rates are typically comparable to or larger than ITG/TEM growth rates. Figure 7(*a*) shows that the simulated local ETG transport ($Q_{\text{e,sim}} \sim 0.1$–$0.3$ MW) is much smaller than experimental transport ($Q_{\text{e,exp}} \sim 2$ MW) and is considerably less stiff than in the example above. Simulations that vary $\nu_e$ independently for each case illustrate the predicted ETG transport is insensitive to variations in electron collisionality as expected from linear stability, which is inconsistent with the global confinement scaling. Instead, simulations at multiple locations that span the high-$k$ measurement region for each discharge ($r/a = 0.56$–$0.71$, figure 7(*b*)) show the predicted transport changes substantially, and around $r/a \sim 0.55$ in the high-$\nu_*$ shot approaches the experimental values. While a number of parameters vary over this region (such as $q$ and $s$, which are known to affect ETG transport through both the linear [60] and nonlinear [83] scalings), the transport variation appears to be most strongly correlated with the density gradient, $a/L_n$.

The sensitivity of ETG turbulence and transport to density gradient has been illustrated in a separate experiment where the

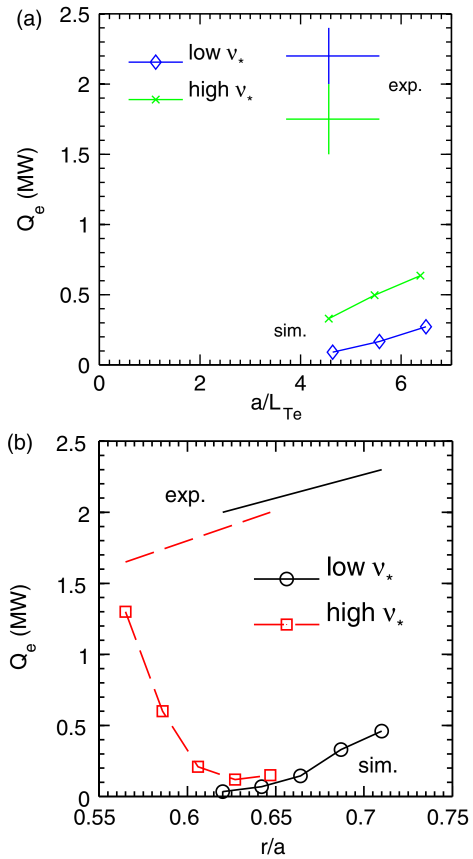


**Figure 7.** (*a*) Nonlinear ETG heat flux versus temperature gradient for low- and high-$\nu_*$ discharges. The experimental values with uncertainties are shown by crosshairs. (*b*) ETG and experimental heat flux versus normalized minor radius ($r/a$).

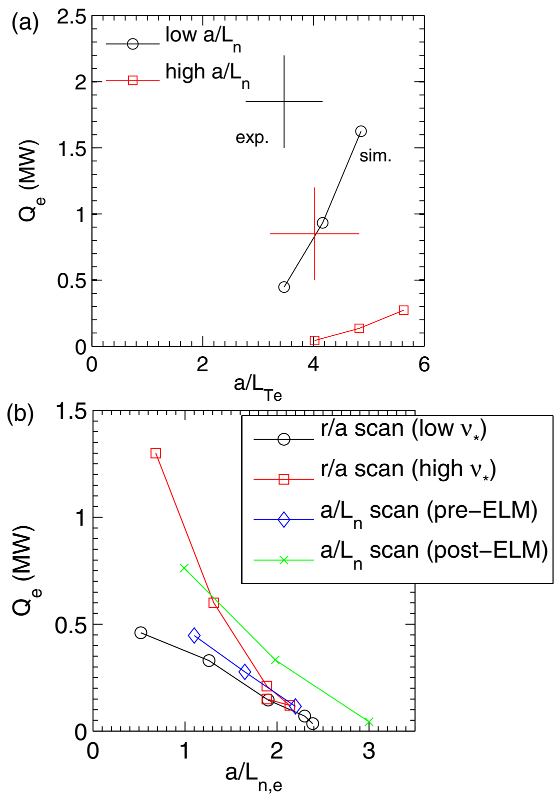


**Figure 8.** (*a*) ETG heat flux versus $a/L_{T_e}$ for low $a/L_{n_e}$ (pre-ELM) and high $a/L_{n_e}$ (post-ELM). (*b*) ETG heat flux versus $a/L_{n_e}$ for pre/post-ELM, also for low/high-$\nu_*$ shots (from $r/a$ scan, figure 7(*b*)).

local core value of $a/L_n$ was increased by a factor ~3–5 as a consequence of a large ELM [62] while other parameters remained relatively constant. Both the measured high-$k$ turbulence spectral power and local electron heat flux was reduced with the increasing $a/L_n$. For the low $a/L_n$ (pre-ELM) parameters, MT modes are stable and low-$k$ ITG/TEM growth rates are comparable to or smaller than $E \times B$ shearing rates. Local nonlinear ETG simulations predict transport approaching the experimental level ($Q_{e,exp} \sim 1.5$–2.2 MW) with ~20% increase in the experimental temperature gradient (figure 8(*a*)). On the other hand, the transport for the high-$a/L_n$ (post-ELM) case is reduced considerably and is much smaller than experiment. (In this case, transport from TEMs, driven by the increased density gradient, may provide a substantial contribution to the total transport [50].)

While the reduction in simulated ETG transport for large $a/L_n$ is partially explained by the higher linear threshold (which can be inferred by extrapolating the predicted heat flux curves in figure 8(*a*) to $Q_e = 0$), there is also a considerable reduction in the stiffness for the larger density gradient. Additional simulations that vary $a/L_n$ separately for each case (figure 8(*b*), circles/squares) confirm that varying density gradient contributes significantly to the variation in predicted ETG transport, consistent with the experimental trend. A very similar dependence of transport versus $a/L_n$ is found when plotting the results from the $r/a$ scan above (figure 7(*b*)), indicating the sensitivity of nonlinear transport to $a/L_n$ which occurs in addition to changes in the linear threshold.

Experiments in NSTX have also investigated the dependence of ETG nonlinear transport with magnetic shear. Electron internal transport barriers (e-ITBs) have previously been reported to occur with strong negative magnetic shear ($s < -0.5$) for RF heated L-mode plasmas [85, 86]. For a large collection of discharges, both the large local electron temperature gradients (much larger than the linear ETG threshold) and the small measured turbulence intensity from 'high-$k$' scattering are strongly correlated with the largest magnitudes of negative magnetic shear. Nonlocal GYRO simulations (that include profile variations) have verified that the ETG turbulence and transport is suppressed with strong negative magnetic shear in the region of the e-ITB, as shown in figure 9 [87]. In the outer regions of the e-ITB ($r/a > 0.3$) the predicted ETG flux reaches experimental levels but turbulence cannot propagate inward past the barrier at min($s$) ($r/a \approx 0.3$).

Additional local simulations ($r/a = 0.3$) at varying magnetic shear verify that this suppression can occur predominantly from a nonlinear stabilizing effect that occurs in the absence of strong $E \times B$ shear, confirming that negative magnetic shear alone is sufficient for ETG suppression. This effect is very strong, with the threshold for significant transport ($R/L_{T_{e,NL}} \sim 12$–18) approaching three times the linear critical gradient ($R/L_{T_{e,lin}} \sim 4$–6) for values of $s$ between $-0.2 \rightarrow -2.4$ (figure 9(*c*)) [87]. This upshift in the effective

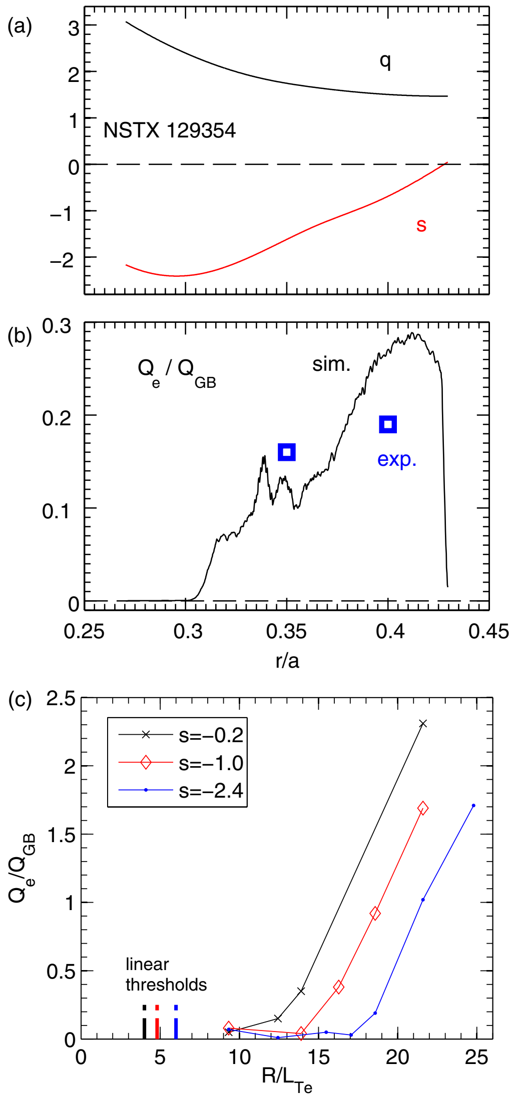


**Figure 9.** ($a$) Safety factor ($q$) and magnetic shear ($s$) profiles for e-ITB discharge. ($b$) ETG electron heat flux from nonlocal simulations. ($c$) ETG heat flux from local simulations varying $R/L_{T_e}$ for varying magnetic shear. The linear thresholds are shown by the vertical dashed lines.

transport threshold is significantly larger than the equivalent 'Dimits' shift that has been predicted in ITG simulations for conventional magnetic shear [88, 89]. We emphasize that in contrast to the cases above where varying density gradient influenced the stiffness of ETG transport, here the strong negative magnetic shear instead influences the effective nonlinear threshold, leaving the stiffness relatively unchanged.

## 5. TEM/KBM turbulence

The analyses presented so far have focused on scenarios and locations where it is reasonable to consider transport mechanisms individually. However, this is often not the case, particularly in high-beta NSTX discharges in the region of $r/a = 0.6$–$0.8$. Figure 10 shows the linear real frequency and growth rate spectra for a lithiated discharge (129041, $r/a = 0.7$) where two ion scale ($k_\theta \rho_s < 1$) modes co-exist (ETG is stable).

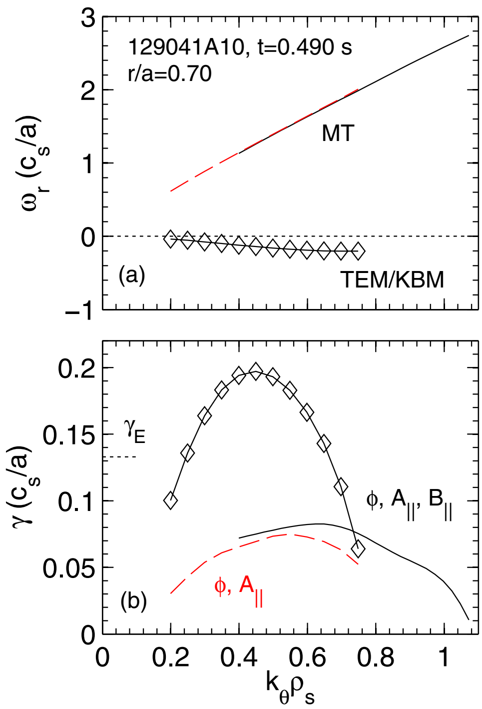


**Figure 10.** ($a$) Real frequency and ($b$) linear growth rate spectra of overlapping MT (lines only) and TEM/KBM (diamonds). Solid (black) lines include $\varphi$, $A_{||}$, $B_{||}$ perturbations while the dashed (red) line includes only $\varphi$, $A_{||}$. Without $B_{||}$ the TEM/KBM mode is stable.

A ballooning mode dominates the linear spectra with growth rates larger than the $E \times B$ shearing rate, peaking around $k_\theta \rho_s \sim 0.45$. A weaker MT mode also exists spanning a broader range of wavenumbers and peaking around $k_\theta \rho_s \sim 0.6$. Overlapping unstable spectra like these have been found in numerous NSTX linear stability simulations (other example spectra are found in [6, 22]) as indicated in figures 1($a$) and ($b$).

The MT mode exhibits the characteristic dispersion in real frequency that closely follows the electron diamagnetic drift frequency ($\omega \approx \omega_{*e} = k_\theta \rho_s \cdot (a/L_n + a/L_{T_e}) \cdot c_s/a$) [22] while the ballooning mode has very small real frequencies in the ion direction. Subsidiary scans using the GYRO eigenvalue solver [42] show the mode growth rate is extremely sensitive to $\beta_e$ (figure 11($d$)) with the appearance of an effective threshold similar to that expected for a KBM instability. However, the KBM mode growth rate never goes to zero, but instead transitions continuously to an extremely weak yet unstable mode that exists even in the electrostatic ($\beta_e = 0$) limit. At the same time, the real frequency changes from the ion drift direction for the experimental value of beta to the electron direction as beta is reduced (figure 11($a$)).

To further probe the nature of this instability, figure 12 shows the $\varphi$, $A_{||}$ and $B_{||}$ eigenfunctions for two values of $\beta_e$. In both cases the mode exhibits ballooning parity as $\varphi$ is symmetric about $\theta = 0$. However, for the experimental beta ($\beta_e = 6.8\%$) the real and imaginary components of $A_{||}$ are out-of-phase, consistent with signatures of KBM [42], while for the reduced $\beta_e$ the $A_{||}$ real/imaginary components are in-phase, consistent with ITG or TEM. A similar continuous transition from KBM to an ITG mode was found previously for collisionless NSTX simulations [42] and was labelled a

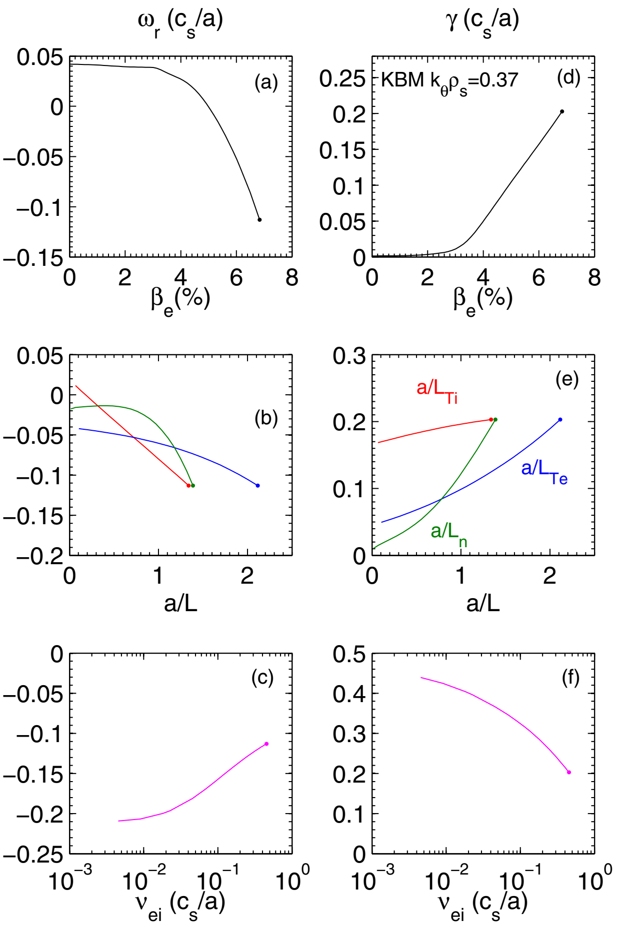


**Figure 11.** Real frequencies (*a*)–(*c*) and growth rates (*d*)–(*f*) for the $k_\theta\rho_s = 0.37$ KBM root using the eigenvalue solver for scans over (*a*), (*d*) $\beta_e$, (*b*), (*e*) $a/L_{T_i}$, $a/L_{T_e}$, $a/L_n$, and (*c*), (*f*) $\nu_{ei}$. Dots represent the experimental parameter values.

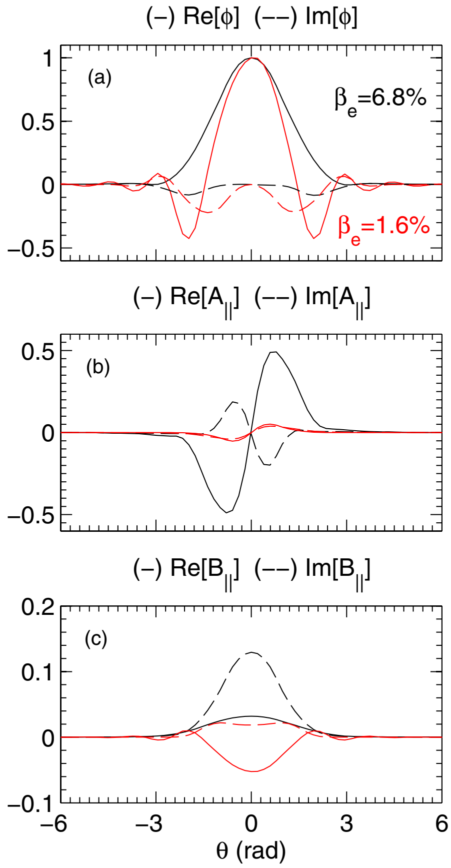


**Figure 12.** (*a*) $\varphi$, (*b*) $A_{||}$ and (*c*) $B_{||}$ eigenfunctions for the $k_\theta\rho_s = 0.37$ mode at both the experimental $\beta_e = 6.8\%$ (black) and reduced $\beta_e = 1.6\%$ (red). Real (imaginary) components are shown by solid (dashed) lines. The real/imaginary phasing of $A_{||}$ changes from KBM at high $\beta_e$ to ITG/TEM at lower $\beta_e$.

'hybrid' ITG/KBM. Given the similar scaling found here, but with a transition to a mode propagating in the electron drift direction at reduced beta, we refer to this mode as a hybrid TEM/KBM.

Additional parameter scans show that, around the base parameters, the KBM is driven unstable most strongly by the density and electron temperature gradients ($a/L_n$, $a/L_{T_e}$), and is weakly dependent on ion temperature gradient, $a/L_{T_i}$ (figure 11(*e*)). Furthermore, the KBM is strongly stabilized by collisions (figure 11(*f*)). The gradient and collisionality scalings are consistent with those found for electrostatic TEM [90], perhaps reinforcing the naming choice as TEM/KBM, although NSTX cases exist where the KBM instability is driven more by the ITG. In any case, we emphasize that around the experimental parameters the mode is effectively a KBM. However, we choose to stick with the 'hybrid' nomenclature to distinguish the unique scaling and continuous transition of this version of KBM. This is to be contrasted with results shown previously for the so-called 'Cyclone base case' [88], where a KBM exists with a definitive threshold in $\beta_e$ ($\gamma_{KBM} \rightarrow 0$), and is distinct from ITG and TEM instability roots that follow separate $\beta_e$ scaling [42, 91–93].

Another unique feature of this KBM mode is that the amplitude of the normalized compressional perturbations, $\delta B_{||}/B_0$, are >10% of the normalized potential perturbations, $e\delta\varphi/T_e$ (figure 12). If compressional magnetic perturbations are neglected in the simulation, the KBM is completely stabilized while the MT mode remains effectively unchanged (figure 10). A similar weakening of instability when neglecting $B_{||}$ at high beta was found previously in STs [42, 73, 74]. (A summary of the influence of $B_{||}$ on different microinstabilities, along with the relation of the equilibrium pressure gradient, has recently been given in [81].) We also note that similar hybrid TEM/KBM behaviour has been predicted in GS2 simulations further out in radius near the top, and inside of, the pedestal region of similar NSTX discharges [35].

One final illustration of the KBM nature of this instability is shown in figure 13, where the growth rates from the separate $\beta_e$ and gradient scans are plotted versus $\alpha_{MHD}$. Note that $\alpha_{MHD}$ can be written as a summation of normalized density, temperature, and gradient of each kinetic species, $s$, $\alpha_{MHD} = q^2(R/a)\beta_{e,unit}\sum_s (n_s/n_e)(T_s/T_e)(a/L_{n_s} + a/L_{T_s})$. Figure 13 shows that the individual parameter scalings are unified by $\alpha_{MHD}$ with an effective threshold around ~0.5 for this case. A similar collapse of $\gamma$ versus $\alpha_{MHD}$ at different radii has been calculated for other discharges, which underlines the correlation illustrated in figure 1(*b*), reinforcing

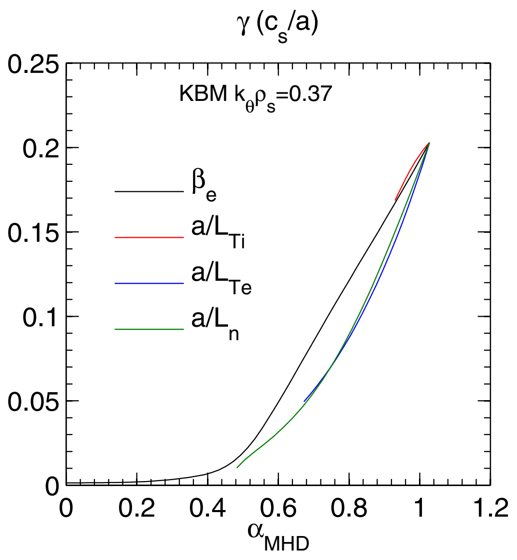


**Figure 13.** Scaling of $k_\theta\rho_s = 0.37$ KBM growth rate versus $\alpha_{\rm MHD}$ for the $\beta_{\rm e}$, $a/L_{T_{\rm i}}$, $a/L_{T_{\rm e}}$ and $a/L_n$ scans shown in figure 11.

that microinstabilities in NSTX can take on a KBM nature in the core confining region. The collisionality dependence also helps explain why the KBM mode is predicted more frequently for lower collisionality conditions in figure 1(*a*). The scaling with collision frequency, opposite to that for MT shown above, suggests that the emergence of hybrid-KBM modes (in the core region) could lead to a change in the overall energy confinement scaling at reduced collisionality [6].

To investigate the nonlinear behaviour of the above hybrid TEM/KBM mode, initial local nonlinear simulations were run including deuterium and carbon, collisions, $\varphi$, $A_{||}$ and $B_{||}$ perturbations. First simulations did not include flow shear, and used the following numerical grid parameters: $L_x \times L_y = 69 \times 63\ \rho_s$, $n_x = 140$, $n_y = 12$, $n_E = 8$, $n_\lambda = 12$, $n_\theta = 14 \times 2$, $\mathrm{d}t = 0.001\ a/c_s$. The simulations show a number of interesting features (figure 14). First, the predicted heat fluxes (~2–4 MW) are experimentally significant ($P_{\rm NBI} \sim 3$ MW) although the transport is very bursty (likely a consequence of the modest perpendicular domain size). Second, there is a significant (~30–40%) contribution to the total heat and particle fluxes from the $B_{||}$ perturbations (rms $\delta B_{||}/B \sim 0.08\%$ for finite $k_\theta$ modes), consistent with the compressional nature of the linear instability discussed above. (See [40] for the exact definition of the calculated flux contributions from each perturbed field quantity.)

The time-averaged transport fluxes peak around $k_\theta\rho_s \sim 0.3$–$0.4$ (figure 14(*c*), solid lines) and decay at higher wavenumbers. The well-defined transport peak and spectral decay appear to be statistically stationary over a relatively long time ($>1000a/c_s$) with no sign of numerical instability. We point out that previous attempts to simulate finite beta turbulence (based around the Cyclone base case) have often found a late-time runaway of heat flux to very large values, as $\beta_{\rm e}$ approaches the KBM threshold [92–94]. Although this phenomenon can appear like a numerical instability, physical processes have recently been proposed to explain it, including the occurrence of a nonlinear subcritical beta limit [94] or a so-called nonzonal transition [95]. In the present case, $\beta_{\rm e}$ is ~2× the KBM threshold and it is unknown why such a similar runaway phenomenon is not observed. It is possible that it reflects the slightly different nature of the hybrid-KBM mode compared to the hard onset of the KBM mode found for Cyclone parameters, but further tests are required to properly understand this. We also point out that quantitative convergence has not been demonstrated; the finite residual values of transport at the highest $k_\theta\rho_s$ (figure 14(*c*)) suggest higher binormal resolution is required for quantitative accuracy. Similar to the MT simulations in section 3, damped buffer boundary regions are used and increased domain width or the use of periodic BCs could also lead to larger quantitative transport.

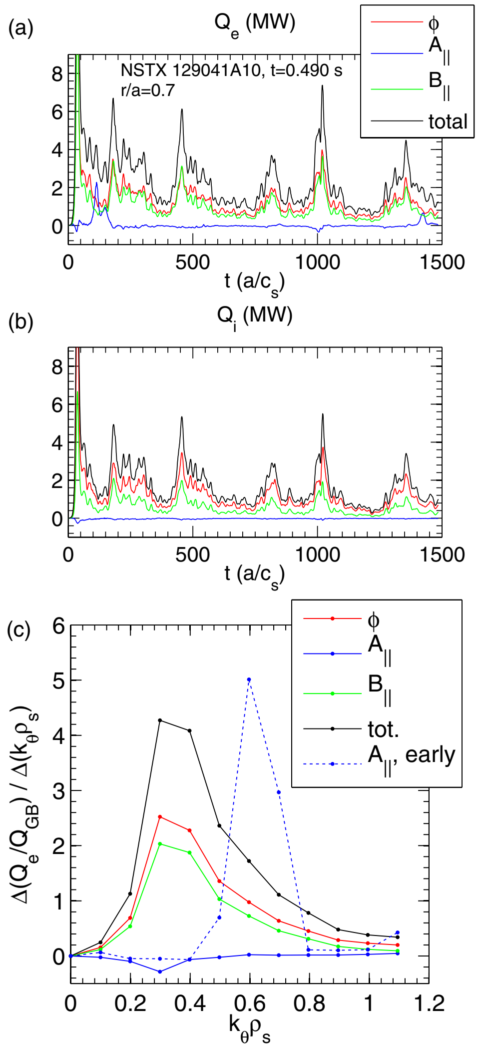


**Figure 14.** Time traces of heat fluxes for electron (*a*) and ion (*b*), separated into contributions from each field. (*c*) Transport spectra for electron heat flux, separated into contributions from each field. Solid lines are time averaged ($t > 300$), the dashed line is $A_{||}$ contribution from MT modes early in the simulation ($t = 150$–$200$).

One can also see around $t = 100$–$150a/c_s$ there is a burst in electron thermal transport from the shear magnetic perturbations ($A_{||}$) which eventually subsides. This burst is absent from other transport channels, and is a consequence of the subdominant MT instability initially growing at higher

$k_\theta\rho_s$, which is apparent from the early time contribution to the $A_{||}$ transport spectra in figure 14(*c*) (the contributions from $\varphi$ and $B_{||}$ are similar to their late time values). In this case the MT turbulence is ultimately unable to compete with the stronger TEM/KBM turbulence. However, the radial resolution employed in these simulations is insufficient to resolve the MT modes at all $k_\theta\rho_s$. For example, the radial grid spacing ($\Delta x = 0.49\rho_s$) is marginally sufficient for representing the MT modes at the peak of the KBM transport spectra ($k_\theta\rho_{s,\max} = 0.3$, $\Delta r_{\rm rat} = 1.86$ for $s = 1.8$), but is likely insufficient to properly resolve the modes at the peak of the MT linear growth rate spectra ($k_\theta\rho_s = 0.6$, $\Delta r_{\rm rat} = 0.93$), which could lead to a reduced linear MT drive [55]. Based on the discussion in section 3 (and [55]), we expect it would take at least 4× the radial resolution ($nx > 600$) to properly resolve all MT modes up to the maximum $k_\theta\rho_s = 1.1$, $\Delta r_{\rm rat} = 0.51$, which will be considered for future simulations.

Finally, it is also interesting to note that when restarting the simulation using the local experimental values of toroidal flow and parallel flow shear ($Ma = 0.23$, $\gamma_{\rm p} = qR/r \cdot \gamma_E = 0.75c_s/a$), the TEM/KBM turbulence predicts finite momentum transport with a Prandtl number $Pr = \chi_\varphi/\chi_{\rm i} \approx 0.4$, although in this particular case the turbulence is strongly reduced if the $E \times B$ shear is also included. Nevertheless, TEM/KBM, or perhaps overlapping TEM/KBM+MT turbulence, provides one possible mechanism that could account for both anomalous electron thermal and momentum transport in NSTX [96]. Within the resolution constraints just discussed, future work will attempt to address how the TEM/KBM and MT modes interact nonlinearly, whether distinct modes can co-exist, and the regimes of nonlinear dominance for each turbulence mechanism.

## 6. Profile effects

The previous sections demonstrated that different theoretical instabilities can dominate in NSTX discharges, which is correlated with local experimental parameters. However, local parameters also vary with minor radius for each discharge, which will naturally influence the strength of each instability, and therefore which particular instability is the strongest. Examples of the former case are shown in figure 7(*b*) for local ETG simulations in the lower beta discharges where the predicted transport varied dramatically with radius.

The situation in the higher beta plasmas is often more complex. Figure 15(*a*) shows the maximum local linear growth rates at four radii between $r/a = 0.6$–$0.8$ for both ion and electron scale instabilities for discharge 129016 discussed in section 4. (Note that the ETG growth rates are normalized to $v_{T_e}/a$ which is $(m_{\rm i}/m_{\rm e})^{1/2} = 60$ times larger than $c_s/a$ used to normalize the ion scale growth rates.) At $r/a = 0.6$, ETG growth rates are very large and the weaker MT mode is expected to be suppressed by the strong $E \times B$ shear, as already discussed in section 4. Further out, the ETG growth rates become much weaker, as does the $E \times B$ shearing rate. Eventually ion scale ballooning instabilities become the strongest modes, behaving like ITG at $r/a = 0.75$ and KBM at $r/a = 0.8$. A second example is shown in figure 15(*b*) for the MT discharge discussed in section 3. Here the MT mode is dominant over the entire $r/a = 0.5$–$0.8$ [22], but the magnitude of the local growth rate increases substantially with radius in comparison to the local $E \times B$ shearing rates. There is also a KBM that begins to compete with MT outside of $r/a > 0.8$.

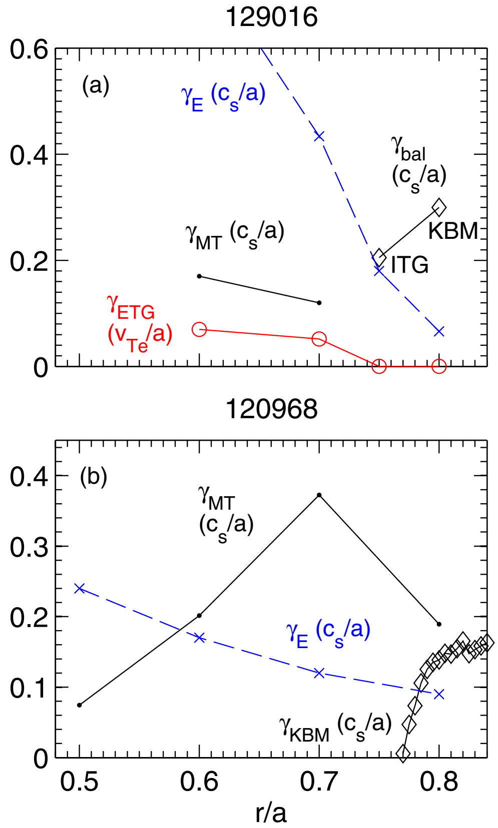


**Figure 15.** Radial profile of maximum linear growth rates for ion scales (MT dots; ballooning diamonds), electron scales (ETG, circles), and $E \times B$ shearing rate (×'s) for (*a*) discharge 129016 (discussed in section 4) and (*b*) 120968 (discussed in section 3). The ballooning mode in 129016 refers to ITG at $r/a = 0.75$ and KBM at $r/a = 0.8$. Note that the ETG growth rates are normalized to the quantity $v_{T_e}/a$ which is $(m_{\rm i}/m_{\rm e})^{1/2} = 60$ times larger than $c_s/a$ used to normalize the ion scale growth rates.

The nonlinear ion scale simulations presented above all use the *local* approximation, i.e. equilibrium quantities ($q$, $n$, $T$ and their gradients) are assumed to be constant across the simulation domain which is typically $L_x = 60$–$120\rho_s$ wide. This is a valid assumption as long as $\rho_* = \rho_s/a$ is very small, such that characteristic turbulence structures (∼ many $\rho_s$) are much smaller than the scale lengths of the profile variations (e.g. $L_{\rm T}$). However, due to the relatively small field strength in STs and corresponding larger values of $\rho_* = \rho_s/a$ ($\rho_{*,\rm unit} = 0.0067$ and $0.0075$ at $r/a = 0.6$ for 129016 and 120968, respectively), the computational domain width is often a significant fraction of the minor radius ($r/a \approx 0.3$–$0.9$). It is very likely that nonlocal [97–99] (and possibly multiscale) effects will be important for simulating the total transport across the radius of these discharges. For example, although the MT simulations at $r/a = 0.6$ discussed in section 3 were suppressed when including $E \times B$ shear, more strongly driven turbulence at $r/a = 0.7$ (where $\gamma_{\rm lin} \sim 2 \times \gamma_E$) could nonlocally enhance transport at $r/a = 0.6$, improving agreement with local experiment analysis. In addition to influencing quantitative transport, in the case illustrated in figure 15(*a*) where different modes appear, global simulations will certainly be required to understand the overall qualitative nature of the resulting turbulence. As mentioned in previous sections, while trying to demonstrate numerical convergence with box size ($L_x$) in a local simulation is useful in the limit of much smaller $\rho_*$, in these NSTX cases it is likely more important to pursue global simulations. Hopefully, fully electromagnetic (shear and compressional), global simulations, especially those capable of resolving MT turbulence, will become feasible in the future with increasing computational power.

## 7. Summary and discussion

There are multiple theoretical turbulence mechanisms that are candidates for explaining the anomalous core electron thermal transport observed in NSTX plasmas owing to the broad range of accessible plasma parameters, such as beta, collisionality and flow shear. Linear gyrokinetic simulations using realistic physics models illustrate trends of when each instability is generally predicted to occur. In high-beta H-mode discharges at ion gyroradius scales, microtearing (MT) modes can be unstable for sufficiently large $a/L_{T_e}$, or $\beta_e \cdot a/L_{T_e}$, while at lower beta traditional electrostatic ion temperature gradient (ITG) and trapped electron modes (TEMs) are unstable. Kinetic ballooning modes (KBMs) are also found unstable in the core confining region but only for sufficiently large normalized pressure gradients, characterized by $\alpha_{MHD}$. While these modes have a very strong dependence on electron beta, they continuously transition from KBM-like to ITG or TEM at reduced beta, so they are referred to as hybrid KBM modes to distinguish them from KBM modes predicted for more conventional tokamak parameters. At electron gyroradius scales the electron temperature gradient (ETG) instability also occurs for sufficiently large $a/L_{T_e}$. For the cases investigated, the occurrence of ETG is also roughly correlated with strong local $E \times B$ shearing rates which is expected to suppress ion scale turbulence.

Nonlinear gyrokinetic simulations have been run for many NSTX discharges in order to validate predictions of the above mechanisms with experimental measurements and to characterize parametric transport dependencies. While it is not always feasible to demonstrate quantitative convergence with numerical resolution, substantial insight can still be inferred from results that have been shown to correctly represent the appropriate physics. In high-beta H-mode plasmas, microtearing simulations predict experimental levels of electron thermal transport entirely from shear magnetic perturbations ($A_{||}$), and a scaling with collisionality consistent with energy confinement scaling regardless of numerical and physical model assumptions. In some high- and low-beta H-modes ETG simulations can also predict significant electron thermal transport. Although ETG transport is independent of collisionality (inconsistent with global confinement scaling) it is found to be sensitive to variations in the local density gradient. Specifically the 'stiffness', or sensitivity of predicted transport to variations in electron temperature gradient, is influenced by the density gradient, an effect which is separate from the known influence of $\nabla n$ on linear ETG stability. In reversed shear L-modes, ETG transport is nonlinearly suppressed by strong negative magnetic shear in the region of observed electron internal transport barriers. In contrast to the influence of the density gradient, the suppression is apparent as an increase in the effective nonlinear threshold, leaving the stiffness relatively unchanged. In high-$\beta$ plasmas with sufficiently large $\alpha_{MHD}$, nonlinear simulations of hybrid TEM/KBM predict significant transport with nearly equal flux contributions from $\varphi$ and $B_{||}$. While weaker microtearing modes are simultaneously unstable in this case, there is very little time-averaged transport associated with the shear magnetic perturbations. Properly resolving all microtearing modes in the simulations remain both expensive and challenging computationally. In addition to energy fluxes, TEM/KBM turbulence also transports particles and momentum, providing a possible mechanism to account for the anomalous momentum transport observed in NSTX plasmas.

While various microinstabilities must be considered in the core of NSTX, the unique scaling dependencies of each turbulence mechanism can hopefully be used to distinguish their behaviours experimentally, especially when using the extended operational range of NSTX Upgrade [58, 59]. One particular parameter of interest is collision frequency, as the three mechanisms focused on in this paper have distinct dependencies: $\chi_e \sim \nu_e^{+1}$ for microtearing, $\chi_e \sim \nu_e^0$ for ETG, and $\gamma_{lin} \sim \nu_e^{-1}$ for TEM/KBM (the transport dependence has yet to be simulated). The overall normalized energy confinement scaling in NSTX discharges $\Omega\tau_E \sim \nu_*^{-0.8}$ is most consistent with microtearing, and the reduced collisionality accessible in NSTX Upgrade will allow for continued investigation of whether the confinement scaling continues to follow this trend. The availability of additional neutral beam sources at different tangency radii in NSTX Upgrade will also allow for manipulation of the safety factor and flow profiles. For conventional safety factor profiles with positive magnetic shear ($s > 0$), ETG tends to be stabilized for larger values of $s/q$ [60]. However, for core NSTX parameters microtearing tends to be destabilized for increasing $s/q$ [22]. Unique to both of these, KBM tends to be destabilized with both increasing q (through $\alpha_{MHD} \sim q^2$) and magnetic shear. Furthermore, varying the local flow profile should alter the strength of ion scale turbulence through the $E \times B$ shearing rates, influencing the relative contribution of ETG turbulence to the electron thermal transport. As the different instability mechanisms can be present simultaneously in a single NSTX discharge, even at the same flux surface location, additional simulations (local, global, and possibly multiscale) will be required to validate how the various mechanisms conspire to produce the experimentally observed energy confinement scalings.

## Acknowledgments

We would like to thank J. Canik, S. Gerhardt and J. Menard for useful discussions. This research used resources of the National Energy Research Scientific Computing Center, supported by US DOE Contract DE-AC02-05CH11231, and the Oak Ridge Leadership Computing Facility, supported by DOE contract DE-AC05-00OR22725. This work was also supported by DOE contracts DE-AC02-09CH11466, DE-FG03-95ER54309, DE-AC52-07NA27344 and DE-FG02-99ER54527.

## References


[1] Peng Y.-K.M. *et al* 2009 *Fusion Sci. Technol.* **56** 957
[2] Voss G.M. *et al* 2008 *Fusion Eng. Des.* **83** 1648
[3] Menard J.E. *et al* 2011 *Nucl. Fusion* **51** 103014
[4] Kaye S.M. *et al* 2007 *Nucl. Fusion* **47** 499
[5] Kaye S.M. *et al* 2007 *Phys. Rev. Lett.* **98** 175002
[6] Kaye S.M. *et al* 2013 *Nucl. Fusion* **53** 063005
[7] Valovič M. *et al* 2009 *Nucl. Fusion* **49** 075016
[8] Valovič M. *et al* 2011 *Nucl. Fusion* **51** 073045
[9] Stutman D. *et al* 2009 *Phys. Rev. Lett.* **102** 115002
[10] Gorelenkov N.N. *et al* 2010 *Nucl. Fusion* **50** 084012
[11] Crocker N.A. *et al* 2011 *Plasma Phys. Control. Fusion* **53** 105001
[12] Coppi B. and Pegoraro F. 1977 *Nucl. Fusion* **17** 969
[13] Kadomtsev B.B. and Pogutse O.P. 1971 *Nucl. Fusion* **11** 67
[14] Lee Y.C. *et al* 1987 *Phys. Fluids* **30** 1331
[15] Hazeltine R.D., Dobrott D. and Wang T.S. 1975 *Phys. Fluids* **18** 1778
[16] Tang W.M., Connor J.W. and Hastie R.J. 1980 *Nucl. Fusion* **20** 1439
[17] Connor J.W., Hastie R.J. and Taylor J.B. 1978 *Phys. Rev. Lett.* **40** 396
[18] Levinton F.M. *et al* 2007 *Phys. Plasmas* **14** 056119
[19] Wong K.L. *et al* 2007 *Phys. Rev. Lett.* **99** 135003
[20] Wong K.L. *et al* 2008 *Phys. Plasmas* **15** 056108
[21] Smith D.R. *et al* 2011 *Plasma Phys. Control. Fusion* **53** 035013
[22] Guttenfelder W. *et al* 2012 *Phys. Plasmas* **19** 022506
[23] Applegate D.J. *et al* 2004 *Phys. Plasmas* **11** 5085
[24] Roach C.M. *et al* 2005 *Plasma Phys. Control. Fusion* **47** B323
[25] Applegate D.J. *et al* 2007 *Plasma Phys. Control. Fusion* **49** 1113
[26] Vermare L. *et al* 2008 *J. Phys.: Conf. Ser.* **123** 012040
[27] Told D. *et al* 2008 *Phys. Plasmas* **15** 102306
[28] Doerk H. *et al* 2012 *Phys. Plasmas* **19** 055907
[29] Petty C.C. *et al* 2012 *Proc. 24th Int. Conf. on Fusion Energy (San Diego, USA, 2012)* (Vienna: IAEA) paper ITR/P1-30
[30] Moradi S. *et al* 2013 *Nucl. Fusion* **53** 063025
[31] Predebon I. *et al* 2010 *Phys. Rev. Lett.* **105** 195001
[32] Carmody D., Pueschel M.J. and Terry P.W. 2013 *Phys. Plasmas* **20** 052110
[33] Dickinson D. *et al* 2011 *Plasma Phys. Control. Fusion* **53** 115010
[34] Dickinson D. *et al* 2012 *Phys. Rev. Lett.* **108** 135002
[35] Canik J.M. et al 2013 Edge plasma transport and microstability analysis with lithium-coated plasma-facing components in NSTX *Nucl. Fusion* submitted
[36] Saarelma S. *et al* 2013 MHD and gyro-kinetic stability of JET pedestals *Nucl. Fusion* submitted
[37] Wong K.L. *et al* 2010 *Bull. Am. Phys. Soc.* **55** 334 (UO4.5)
[38] Scott B.D. 2003 *Plasma Phys. Control. Fusion* **45** A385
[39] Kinsey J.E. *et al* 2011 *Nucl. Fusion* **51** 083001
[40] Candy J. and Belli E. 2010 *General Atomics Technical Report* No GA-A26818
[41] Candy J. and Waltz R.E. 2003 *J. Comput. Phys.* **186** 545
[42] Belli E. and Candy J. 2010 *Phys. Plasmas* **17** 112314
[43] Candy J. 2009 *Plasma Phys. Control. Fusion* **51** 105009
[44] Canik J.M. *et al* 2011 *Phys. Plasmas* **18** 056118
[45] Maingi R. *et al* 2011 *Phys. Rev. Lett.* **107** 145004
[46] Boyle D.P. *et al* 2011 *Plasma Phys. Control. Fusion* **53** 105011
[47] Maingi R. *et al* 2012 *Nucl. Fusion* **52** 083001
[48] Gray T. *et al* 2013 The effects of increasing lithium deposition on the power exhaust channel in NSTX *Nucl. Fusion* submitted
[49] Gerhardt S. *et al* 2011 *Nucl. Fusion* **51** 073031
[50] Ren Y. *et al* 2012 *Phys. Plasmas* **19** 056125
[51] Ren Y. *et al* 2013 *Nucl. Fusion* **53** 083007
[52] Drake J.F. and Lee Y.C. 1977 *Phys. Fluids* **20** 1341
[53] Gladd N.T., Drake J.F., Chang C.L. and Liu C.S. 1980 *Phys. Fluids* **23** 1182
[54] Hassam A.B. 1980 *Phys. Fluids* **23** 2493
[55] Guttenfelder W. *et al* 2012 *Phys. Plasmas* **19** 056119
[56] Groebner R.J. *et al* 2010 *Nucl. Fusion* **50** 064002
[57] Snyder P.B. *et al* 2011 *Nucl. Fusion* **51** 103016
[58] Menard J.E. *et al* 2012 *Nucl. Fusion* **52** 083015
[59] Gerhardt S.P. *et al* 2012 *Nucl. Fusion* **52** 083020
[60] Jenko F. *et al* 2001 *Phys. Plasmas* **8** 4096
[61] Mazzucato E. *et al* 2008 *Phys. Rev. Lett.* **101** 075001
[62] Ren Y. *et al* 2011 *Phys. Rev. Lett.* **106** 165005
[63] Waltz R.E. *et al* 1994 *Phys. Plasmas* **1** 2229
[64] Kinsey J., Waltz R. and Candy J. 2007 *Phys. Plasmas* **14** 102306
[65] Guttenfelder W. *et al* 2011 *Phys. Rev. Lett.* **106** 155004
[66] Doerk H., Jenko F., Pueschel M.J. and Hatch D.R. 2011 *Phys. Rev. Lett.* **106** 155003
[67] Wang E. *et al* 2011 *Phys. Plasmas* **18** 056111
[68] Rechester A.B. and Rosenbluth M.N. 1978 *Phys. Rev. Lett.* **40** 38
[69] Zhang J. *et al* 2010 *Rev. Sci. Instrum.* **81** 10D519
[70] Zhang J. *et al* 2013 *Plasma Phys. Control. Fusion* **55** 045011
[71] Applegate D. 2006 Gyrokinetic studies of a spherical tokamak H-mode plasma *PhD Thesis* Imperial College London
[72] Hawryluk R.J. 1979 *Proc. Course on Physics of Plasmas Close to Thermonuclear Conditions (Varenna, Italy, 1979)* vol 1, p 19
[73] Kotschenreuther M. *et al* 2000 *Nucl. Fusion* **40** 677
[74] Bourdelle C. *et al* 2003 *Phys. Plasmas* **10** 2881
[75] Rewoldt G., Tang W.M., Kaye S. and Menard J. 1996 *Phys. Plasmas* **3** 1667
[76] Drake J.F., Gladd N.T., Liu C.S. and Chang C.L. 1980 *Phys. Rev. Lett.* **44** 994
[77] Dominguez R.R., Rosenberg M. and Chang C.S. 1981 *Phys. Fluids* **24** 472
[78] Craddock G.G. and Terry P.W. 1991 *Phys. Fluids* B **3** 3286
[79] Guttenfelder W. and Candy J. 2011 *Phys. Plasmas* **18** 022506
[80] Roach C.M. *et al* 2009 *Plasma Phys. Control. Fusion* **51** 124020
[81] Joiner N., Hirose A. and Dorland W. 2010 *Phys. Plasmas* **17** 072104
[82] Holland C. *et al* 2011 *Phys. Plasmas* **18** 056113
[83] Jenko F. and Dorland W. 2002 *Phys. Rev. Lett.* **89** 225001
[84] Smith D.R. *et al* 2008 *Rev. Sci. Instrum.* **79** 123501
[85] Yuh H. *et al* 2011 *Phys. Rev. Lett.* **106** 055003
[86] Yuh H. *et al* 2009 *Phys. Plasmas* **16** 056120
[87] Peterson J.L. *et al* 2012 *Phys. Plasmas* **19** 056120
[88] Dimits A. *et al* 2000 *Phys. Plasmas* **7** 969
[89] Mikkelsen D.R. and Dorland W. 2008 *Phys. Rev. Lett.* **101** 135003
[90] Peeters A.G. *et al* 2005 *Phys. Plasmas* **12** 022505
[91] Candy J. 2005 *Phys. Plasmas* **12** 072307
[92] Pueschel M.J., Kammerer M. and Jenko F. 2008 *Phys. Plasmas* **15** 102310
[93] Pueschel M.J. and Jenko F. 2010 *Phys. Plasmas* **17** 062307
[94] Waltz R.E. 2010 *Phys. Plasmas* **17** 072501
[95] Pueschel M.J. *et al* 2013 *Phys. Rev. Lett.* **110** 155005
[96] Kaye S.M. *et al* 2009 *Nucl. Fusion* **49** 045010
[97] Hahm T.S. *et al* 2004 *Plasma Phys. Control. Fusion* **46** A323
[98] Waltz R.E. and Candy J. 2005 *Phys. Plasmas* **12** 072303
[99] Görler T. *et al* 2011 *Phys. Plasmas* **18** 056103